



HAL
open science

Salt storage and induced crystallisation in porous asymmetric inorganic membranes

Weng Fu, Julius Motuzas, David Wang, Christelle Yacou, Anne Julbe, James Vaughan, João Diniz da Costa

► **To cite this version:**

Weng Fu, Julius Motuzas, David Wang, Christelle Yacou, Anne Julbe, et al.. Salt storage and induced crystallisation in porous asymmetric inorganic membranes. *Journal of Membrane Science*, 2022, 641, pp.119872. 10.1016/j.memsci.2021.119872 . hal-03371555

HAL Id: hal-03371555

<https://hal.science/hal-03371555v1>

Submitted on 8 Oct 2021

HAL is a multi-disciplinary open access archive for the deposit and dissemination of scientific research documents, whether they are published or not. The documents may come from teaching and research institutions in France or abroad, or from public or private research centers.

L'archive ouverte pluridisciplinaire **HAL**, est destinée au dépôt et à la diffusion de documents scientifiques de niveau recherche, publiés ou non, émanant des établissements d'enseignement et de recherche français ou étrangers, des laboratoires publics ou privés.

Salt Storage and Induced Crystallisation in Porous Asymmetric Inorganic Membranes

Weng Fu^{1,2}, Julius Motuzas¹, David Wang^{1,3}, Christelle Yacou^{1,4}, Anne Julbe⁵, James Vaughan^{2*},
João C. Diniz da Costa^{1,6,7}

¹ The University of Queensland, FIM²Lab – Functional Inorganic Materials and Membrane Laboratory, School of Chemical Engineering, Brisbane Qld 4072, Australia.

² The University of Queensland, Hydrometallurgy Research Group, School of Chemical Engineering, Brisbane Qld 4072, Australia.

³ The University of Sydney, School of Chemical and Biomolecular Engineering, Sydney NSW 2006, Australia.

⁴ Université des Antilles, Department of Engineering, BP 250, 97157 Pointe à Pitre Cedex, Guadeloupe, France.

⁵ Institut Européen des Membranes (IEM, UMR 5635 CNRS, ENCM, UM), Université de Montpellier, CC47, Place Eugène Bataillon, 34095 Montpellier Cedex 5, France.

⁶ LAQV-REQUIMTE, (Bio)Chemical Process Engineering, Department of Chemistry, Faculty of Science and Technology, Universidade NOVA de Lisboa, 2829-516 Caparica, Portugal.

⁷ iBET – Instituto de Biologia Experimental e Tecnológica, 2781-901 Oeiras, Portugal

*Corresponding authors: JV (james.vaughan@uq.edu.au)

Abstract

Processing brines to recover strategic mineral salts using evaporation ponds requires large surface areas and are slow, even in arid climates. Here we show a novel membrane macropore storage mechanism that induces fast salt crystallisation in mesoporous top-layers in inorganic asymmetric membranes, stemming from 789 million nucleation points per metre square of surface area. During membrane pervaporation, dissolved salts are retained mainly in the macropores of the substrate which subsequently provide ideal conditions for crystal nucleation and growth on the membrane surface upon drying. This novel pore storage mechanism is attained owing to the solution flow modulation of the mesoporous titania and gamma-alumina layers that is counterbalanced by the flow of water during pervaporation. Therefore, pore size control is imperative to avoid flooding in the macroporous substrate. This work further shows the fundamental properties of the salt storage mechanism described by a single salt production coefficient, and a global salt production coefficient for metal chloride salts. This technology could potentially be considered for unlocking and process strategic global minerals from brines.

Key words: inorganic membranes; pore storage; pore size control; pervaporation; crystallisation.

1. Introduction

The demand for strategic minerals to meet our contemporary societies need for technological advancement is expanding. Meanwhile, conventional orebody grades are in decline, thus mineral brine mines will be an increasingly important source of salts and metals in the future. A clear example

41 is lithium, a relatively rare metal required for the production of highly efficient batteries for portable
42 electronic devices [1], plug-in electrical cars [2] and increasingly for large scale power storage [3].
43 The estimated global lithium brine reserves of 21.6 Mt is 5.6 times larger than non-brine lithium
44 reserves [4]. Even larger reserves are the oceans of the world which are last frontier in mineral
45 processing, holding vast quantities of dissolved metal ions of commercial interest, such as lithium
46 (2.3×10^5 Mt), nickel (8,600 Mt), magnesium (1.3×10^{12} Mt), gold (14.5 Mt), potassium (5.1×10^8 Mt),
47 manganese (500 Mt) and uranium (4,300 Mt) among many others [5]. These elements find broad
48 application in wealth generation (gold), and advanced materials such as magnesium for medical
49 applications [6], manganese doped semiconductor quantum dots [7] and nickel as catalyst [8]. In
50 addition, potassium plays a critical role in food production [9] and uranium is a key element to nuclear
51 power production in a decarbonised economy [10]. However, extracting valuable elements from
52 mineral brines is time and energy intensive and expensive, particularly in the case of diluted metal
53 ions in oceans [11].

54
55 Mineral brines are traditionally processed in evaporation ponds and industrial crystallisers.
56 Essentially these processes evaporate water from a brine solution, leading to supersaturation and
57 crystallisation. The crystallisation of evaporation ponds is very slow and highly dependable upon the
58 weather conditions whilst industrial crystallisers deliver fast crystallisation rates though are energy
59 intensive. Since the 1980s, polymeric hydrophobic membranes have become attractive to promote
60 crystal nucleation and growth kinetics [12], using membrane distillation, also known as
61 pervaporation. This process is known as membrane crystallisation, with proven applications for
62 crystallising LiCl [13], NaCl [14, 15], Na_2CO_3 [16] and MgSO_4 [17]. Owing to the fast pervaporation
63 of solvent via the hydrophobic polymeric membrane, ideal conditions are created at surface of the
64 membrane at the feed side, leading to supersaturation, nucleation and crystallisation. Subsequently,
65 two further downstream processes are required where (i) crystals are separated from the solution by
66 filters and then (ii) dried in furnaces.

67

68 Although the state of the art in polymeric membrane crystallisation is well known, inorganic ceramic
69 membranes remained absent [18] in this technological development until recently by the pioneering
70 work of Motuzas and co-workers [19] who prepared porous hydrophobic carbon membranes to
71 crystallise NaCl from mineral brine solutions. This process is known as membrane percrystallisation
72 as solutes (i.e., crystals) and solvents were separated at a single step by a wet thin film under vacuum
73 on the permeate side of the membrane. Subsequently, it was demonstrated that the process conditions
74 (i.e., flow rates, temperature and vacuum pressure) in membrane percrystallisation altered the crystal
75 NaCl particle size [20], and the crystal phase of NiSO₄ [21]. The use of hydrophilic inorganic
76 membranes has eluded the field of membrane crystallisation to date.

77

78 Therefore, this work demonstrates for the first time that hydrophilic inorganic membranes can be
79 used efficiently for crystallising mineral brines by a novel pore storage mechanism under
80 pervaporation. It is shown that salt storage in the macropores of a ceramic membrane substrate under
81 pervaporation can be attained only in the presence of a mesoporous inorganic top-layer with
82 controlled pore sizes. Further, this work demonstrates that fundamental mass transfer properties in
83 the pore storage are a function of feed concentrations for a single salt, and as a function of the
84 molecular weight for chloride salts.

85

86 **2. Experimental**

87 **2.1 Sol-gel synthesis and xerogel characterisation**

88 An aqueous aluminium oxide (20%) sol with an average colloidal particle size of 0.05 µm (pseudo-
89 boehmite from Alfa Aesar) was used as received for coating gamma alumina interlayers. The top
90 layers were synthesised using a titania sol-gel method. Briefly, titanium (IV) isopropoxide (TIP,
91 TiC₁₂H₂₈O₄, 98%, Sigma-Aldrich) was added drop-wise into a solution of double-distilled water and
92 hydrochloric acid under vigorous stirring. Then the mixture was maintained in a water bath at 30 °C

93 for 3 hours. The molar ratio of the final sol was TIP:HCl:H₂O = 1:1:22. The sol was then dried in an
94 oven at 60 °C for 3 h.

95

96 The preparation of xerogel (dried gel) was initially carried out by heat treatment at 150 °C to ensure
97 the consolidation of the titania matrix. Subsequently, the titania xerogel was calcined at 350 °C to
98 condense the matrix into a meso-structure. Heat treatment and calcination were carried out at a
99 heating/cooling rate of 1 °C min⁻¹ and a dwell time of 1 h. Nitrogen sorption of titania xerogel samples
100 was conducted on a Micromeritics TriStar 3020 analyser after degassing under vacuum on a
101 Micromeritics VacPrep061 at 200 °C for a minimum of 12 h. The specific surface areas were
102 calculated from the adsorption isotherms via the multi-points BET model at relative pressures
103 of $p/p_0=0.05-0.3$. The pore size distribution was determined using Barrett–Joyner–Halenda (BJH)
104 model, from the desorption branch of the isotherms of the mesoporous titania xerogel samples.

105

106 **2.2 Membrane preparation and characterisation**

107 Commercial porous alpha alumina (α -Al₂O₃) tubes (OD = 1 cm, ID = 0.5 cm, L = 5.5 cm, Ceramic
108 Oxide Fabricator Pty Ltd.) were used as membrane substrates. The substrates were pre-calcined at
109 1000 °C for 8 h with a ramp rate of 5 °C min⁻¹ to improve the mechanical strength and to remove any
110 organic impurities. Each coated layer was deposited separately by a dip-coating method at immersion
111 and withdrawal rate of 5 cm min⁻¹ and a dwell time of 1 min. Both ends of the substrate were closed
112 prior to dip-coating to allow layers to be coated on the outer shell of the substrate only. After each
113 coated layer, the membranes were calcined in air at 500 °C (gamma alumina interlayers), 150 and
114 350 °C (titania top layers) at a ramping/cooling rate of 1 °C min⁻¹ and a dwell time of 1 h. The latter
115 followed a procedure proposed by Yacou et al. [22] in order to control the mesopore size of titania
116 thin films. The final prepared membranes consisted of two gamma alumina interlayers and two titania
117 top layers. Microstructural investigation of the membrane layers was carried out via a JEOL field

118 emission scanning electron microscope (FE-SEM, JEOL JSM-7001F) operating at 5 kV at a working
119 distance of 10 mm.

120

121 **2.3 Membrane crystallisation**

122 Synthetic feed solutions were prepared by mixing chloride based salts (mol_s) with the required amount
123 of double-distilled water (L_w) represented by $\text{mol}_s L_w^{-1}$. The salt concentration of the feed solution
124 was determined via standard calibration curves (conductivity versus concentration) using a
125 conductivity meter (labCHEM CP). The membrane outer shell was exposed to a pre-determined salty
126 feed solution at atmospheric pressure and room temperature ($\sim 20^\circ\text{C}$). The inner shell of the
127 membrane (i.e., permeate side) was evacuated to 18 mbar using a vacuum pump, thus allowing water
128 to evaporate and salt to remain in the pores of the membrane. The effective length of the membrane
129 for pervaporation testing was 4.5 cm, as 0.5 cm at both ends of the substrate were covered with silicon
130 tubes. The membranes were tested at time intervals from 10 to 30 min. The water vapour in the
131 permeate stream was condensed and collected in a liquid nitrogen cold trap located downstream. The
132 collected water was analysed using the conductivity meter to determine if any salt ions were entrained
133 in the water vapour during water evaporation.

134

135 After testing, the membranes were transferred to a pre-heated oven at 60°C for 8 h to ensure a
136 complete crystallization of salts on the TiO_2 top layer took place on the outer shell of the membrane.
137 The pervaporation schematic and salt growth on the membrane surface is depicted in the Appendix
138 Fig. A1. The relative humidity of the oven chamber ($\text{RH} = 67.3\%$) was controlled using NaNO_3 brine
139 solution. Salt crystals on the surface of the membranes were observed with JEOL field emission
140 scanning electron microscope (FE-SEM, JEOL JSM-7001F) operating at 5 kV at a working distance
141 of 10 mm.

142

143 The crystallised salts were removed from the outer surface of the membrane and the collected mass
144 of salt crystals was measured in a high-precision laboratory scale. This allowed the production (J) of
145 crystallised salts to be determined as follows,

$$146 \quad J = \frac{m_{salt}}{tA} \quad (Eq. 1)$$

147 where m_{salt} is the mass of crystallised salt collected at a pre-determined membrane pervaporation time
148 interval t (min), and A (m^2) is membrane surface area. The membrane pervaporation followed by
149 oven drying were replicated at least five times for all tested conditions. A Panasonic microwave
150 (Genius 1100 MW) with variable power was also used for drying and crystallising chloride base salts.
151 The membranes were microwave-dried at 900 W for 2 min. The mass and flux of crystallised chloride
152 base salts after microwave-dried were calculated using a similar procedure as described above for the
153 oven-dried membranes.

154

155 **3. Results and discussion**

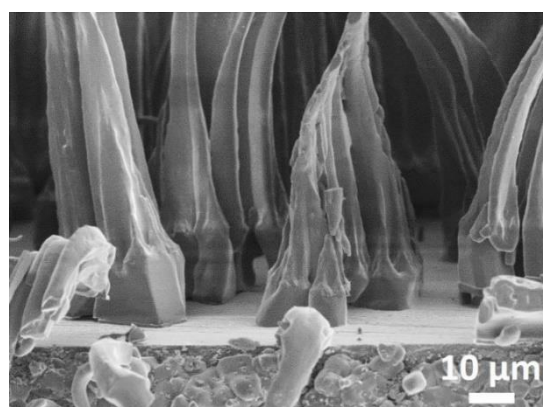
156 **3.1 Induced Crystallisation and Membrane Characteristics**

157 Here we demonstrate for the first time that hydrophilic inorganic ceramic membranes are very
158 efficient in processing mineral brines by a novel mechanism of induced salt crystallisation. We
159 observed that under pervaporation of an aqueous NaCl solution, salts concentrated in the pores whilst
160 water permeated through the membrane. Upon drying the membrane, capillary forces in the pores
161 induced evaporation of water, leading to super-saturation, nucleation and crystal growth on the
162 surface of the membrane. Fig. 1 displays NaCl crystals grown perpendicular to the membrane surface
163 which appear as a salt crystal forest-type arrangement. The crystals are unusual, having a cubic shaped
164 base at the interface of the membrane followed by an elongated pyramid shape, in sharp contrast to
165 conventional NaCl cubic crystals. It is noteworthy that the crystals are approximately equidistant
166 from each other.

167

168 Analysis of the SEM image (Fig. 1) suggests that the base of the crystal is of $\sim 20.5 (\pm 2) \mu\text{m}$, and the
169 average distance between each crystal base is $\sim 15.1 (\pm 1.5) \mu\text{m}$. Therefore, one square metre of
170 inorganic membrane area generates on the order of 789 million nucleation points of these unusual
171 crystals in a single processing cycle of pervaporation, pore storage and crystallisation. As salt ions
172 are expelled from the pores of the membrane, their concentration increases on the surface of the
173 membrane. This process of mass transfer leads to spontaneous crystal nucleation in a supersaturated
174 thin wet film on the surface of the membrane. Upon formation of the stable nuclei, crystal growth
175 predominates which lowers the local supersaturation and inhibits further nucleation. Consequently,
176 salt ions diffuse on the surface of the membrane from areas of high concentration to low concentration
177 due to the chemical potential, thus favouring crystal growth.

178



179

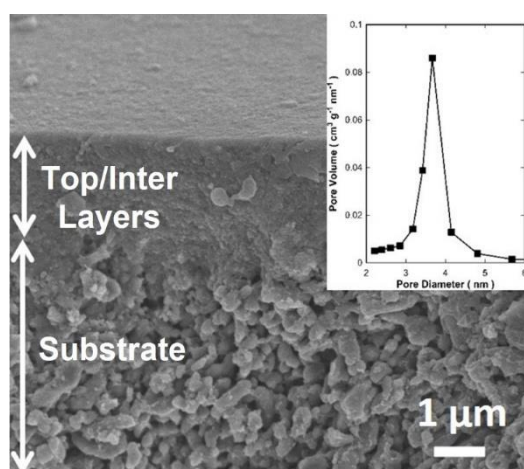
180 Fig. 1. SEM image of NaCl crystal pyramid-like shapes on a membrane dried at 60 °C.

181

182 Induced salt crystallisation occurred in asymmetric membranes (see representative SEM image in
183 Fig. 2) composed of two top layers (titania) and two interlayers (gamma-alumina) with a combined
184 average thickness of 1.95 μm coated on an alpha-alumina support. The asymmetric configuration is
185 based on the principle that the thin top layers are coated on a mechanically strong substrate, whilst
186 the interlayer provides a smooth surface to form a defect free thin top layer [23]. A fundamental
187 aspect of this induced pore crystallisation is the precise control of the sol-gel method to tailor the
188 inorganic hydrophilic membrane pore diameter (d_p). This was achieved by an acid sol-gel synthesis

189 of the titania top layers followed by a two-step calcination to 150 and 350 °C and using a low ramping
190 rate of 1 °C min⁻¹. A number of hydrophilic membranes were tested under pervaporation of aqueous
191 NaCl solutions. The pore size of macroporous alpha alumina ($d_p > 50$ nm) were too large, resulting
192 in pore wetting and full permeation of the solution. In the case of microporous silica membranes (d_p
193 < 0.5 nm or 5 Å) [24], only water diffused through the membranes as the permeation of salt ions were
194 hindered. Pore storage was observed for mesoporous titania top-layers ($3 < d_p < 5$ nm) (Fig. 2 inset)
195 and gamma alumina ($3.7 < d_p < 8.9$ nm) [25] interlayers.

196



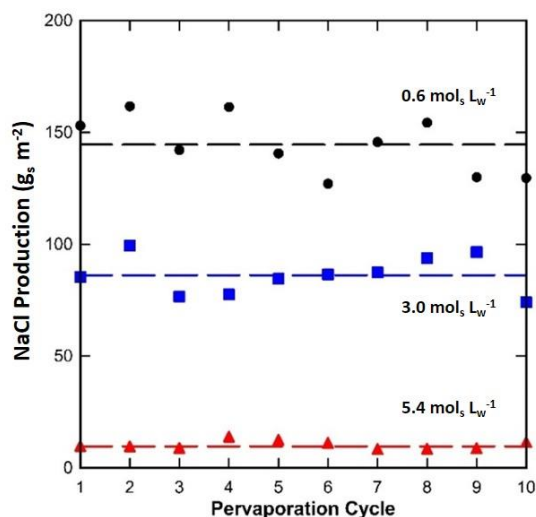
197

198 Fig. 2. SEM image of an asymmetric titania (top-layer) and gamma alumina (interlayer) where inset
199 shows a pore size distribution based on Barrett, Joyner and Halenda (BJH) model.

200

201 3.2 Membrane Performance

202 Fig. 3 shows the stable cyclic performance of the titania/alumina membrane over 10 consecutive
203 cycles of pervaporation and NaCl crystallisation. Increasing the NaCl feed concentration resulted in
204 an increase in the production of NaCl crystals, suggesting an increase in the storage rate of NaCl in
205 the pores of the membranes. Notably, the titania/alumina membrane was able to process a wide range
206 of feed solution concentrations ranging from seawater (0.6 mol_s L_w⁻¹ NaCl) to hypersaline brines (5.4
207 mol_s L_w⁻¹ NaCl).

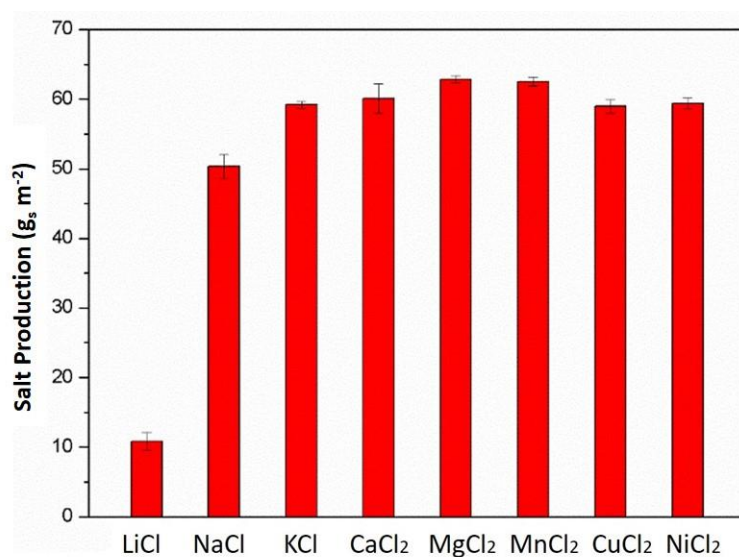


208

209 Fig. 3 NaCl production rate for 10 successive cycles of pervaporation of 30 min for various NaCl
 210 feed concentrations (0.6, 3.0 and 5.4 mol_s L_w⁻¹). The membranes were oven-dried at 60 °C for 8 h
 211 and RH = 67.3%.
 212

213 This novel induced crystallisation proved to be very effective for a number of chloride salts as
 214 displayed in Fig. 4. Under cycles of pervaporation of 10 min, the salt storage in the nanopores varied
 215 between 50 to 63 g m⁻², except for LiCl. It was observed that Li had reacted slightly with the
 216 membrane as the top layer became darker instead of the typical white titania colour. The Li reaction
 217 along with the relatively low molar mass of Li explains the lower LiCl storage per cycle.

218



219

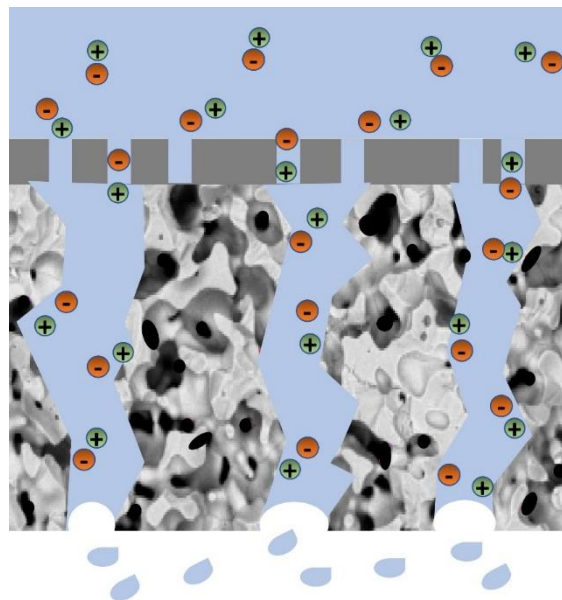
220 Fig. 4. Chloride salt production for feed concentrations (3 mol_s L_w⁻¹) at 20 °C with a pervaporation
 221 time of 10 min. The membranes were microwave-dried at 900W for 2 min. Salt production includes
 222 hydrated salts.

223


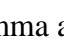



224 3.3 Novel pore storage mechanism

225 Salt crystallisation on the membrane surface proceeded via pervaporation as schematically depicted
226 in Fig. 5. Upon contact of the dry membrane with an aqueous salt solution, capillary forces take effect
227 immediately [26]. These forces induced salt solution penetration into the pores due to the hydrophilic
228 nature of titania and gamma-alumina layers. Based on the results in Fig. 3 for a feed solution of 5.4
229 mol_s L_w⁻¹, the NaCl production average is 144.5 g m⁻². This is equivalent to a NaCl crust of NaCl with
230 a thickness of 67 μm. The latter is 35 times thicker than the average thickness of the mesoporous
231 titania and gamma-alumina layers of 1.95 μm. Therefore, the mass of salt that causes induced
232 crystallisation can be directly attributed to salt storage in the membrane substrate that accounts to
233 99.96% of the overall membrane thickness. Theoretical calculations in the Appendix Table A1 clearly
234 confirms that this is the case as there is sufficient pore volume in the membrane substrate to
235 accommodate the NaCl mass that induced crystallisation.

236



237

238 Fig. 5. Idealised schematic representing the salt storage in the membrane where  is the salt feed
239 solution,  is the titania and gamma alumina mesoporous layers,  is the water meniscus,  is
240 water vapour and  is the alpha alumina macroporous substrate.
241

242 It is noteworthy the role played by the mesoporous titania and gamma-alumina layers in avoiding
243 membrane flooding under pervaporation. In this case, the mesoporous layers modulated the flow of
244 salt ion solution into the larger macropores of the substrate. This flow modulation benefited the salt
245 storage mechanism by entraining salt ions in the macropores of the substrate whilst avoiding solution
246 flooding in the permeate side.

247

248 In this process, menisci are formed in the macropores of the substrate close to the surface of the inner
249 shell of the tubes under pervaporation, thus controlling the water evaporation via the permeate stream.
250 The water evaporation at the menisci is controlled by vapour-liquid equilibrium according to the
251 Kelvin equation [27]. The water pervaporated through the membrane was condensed in a liquid
252 nitrogen cold trap and analyses indicated salt rejections in excess of 99%, confirming that salt ion
253 solution was mainly retained in the macropores of the substrate of the membrane.

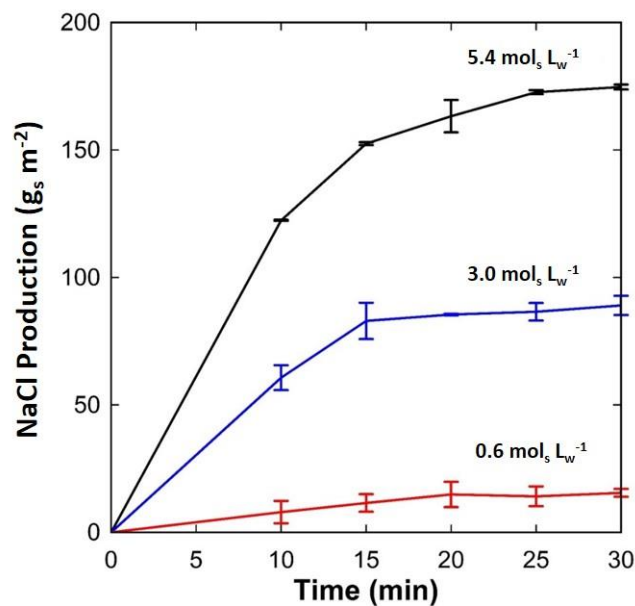
254

255 Upon drying the membrane, induced salt crystallisation on the surface of the mesoporous titania top
256 layer took place. This process is directly controlled by capillary forces. As the macropores of the
257 alpha-alumina substrate are interconnected to the mesopores of gamma-alumina interlayers and that
258 to the mesopores of the titania layer, capillary pressure gradients force the salt ion solution stored in
259 the substrate to permeate from the macropores to the mesopores. This is the case for two different
260 saturated porous materials in hydraulic contact with each other and dried, the material with the largest
261 pores starts to drain first [28]. Upon drying further, capillary forces bring the salt ion solution to the
262 surface of the titania top layer where water evaporation increases rapidly. As a result, salt ions on the
263 membrane surface reach supersaturation and lead to salt nucleation and salt growth induction as
264 evidenced by Fig. 1.

265

266 **3.4 Transport phenomena, salt production and storage coefficients**

267 During the pervaporation stage, salt is being concentrated in the membrane pores (c_p) as the process
 268 is driven by vacuum evaporation of water. A concentration gradient (Δc) is thus established between
 269 the solution in the membrane pores and the solution in the feed. Fig. 6 shows the continuous built up
 270 of NaCl in the membrane pores as a function of time until a maximum salt storage capacity is reached.
 271 At this maximum capacity, the pores are fully saturated with salt solution and equilibrium is achieved
 272 between the salt concentration in the feed solution and that in the macropores. In addition, the salt
 273 production capacity also increased as a function of the NaCl feed concentration. Hence, the transport
 274 phenomenon in this membrane pore storage mechanism is associated with the salt concentration in
 275 the feed solution. The driving force for salt storage is at the highest at the beginning of pervaporation
 276 ($t=0$) and minimum at the maximum storage or saturation time ($t=t_{sat}$). In other words, the membrane
 277 pore storage mechanism is characterised by a batch process of salt loading.



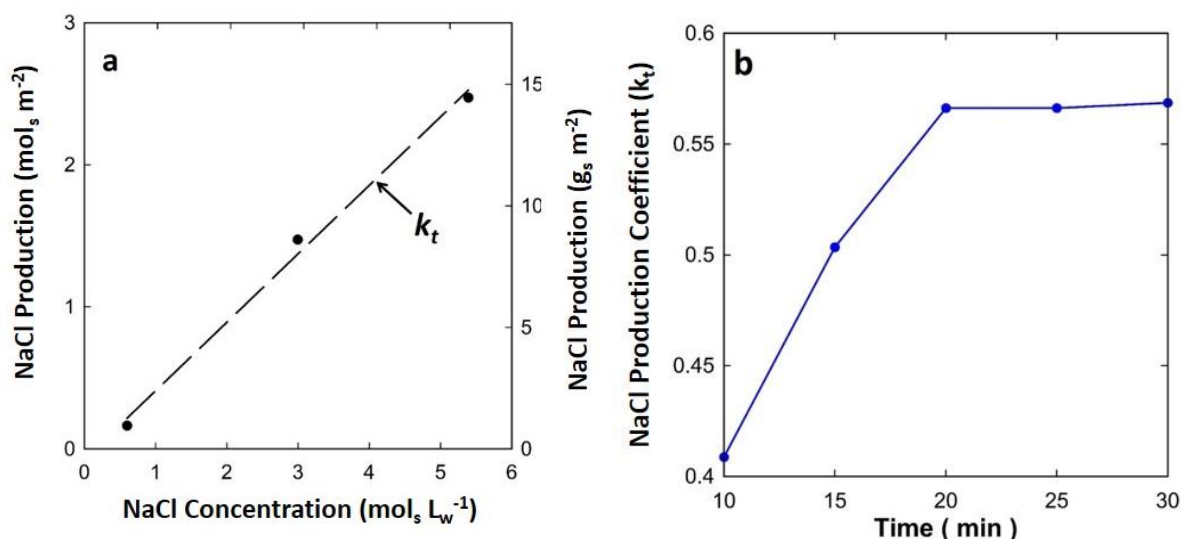
278
 279 Fig. 6. NaCl production as a function of pervaporation time for a porous membrane tube thickness
 280 of 2.5 mm for various NaCl feed concentration (0.6, 3.0 and 5.4 mol_s L_w⁻¹). The membranes were
 281 oven dried at 60 °C for 8 h and RH = 67.3%.
 282

283 Interestingly, the production of NaCl as a function of the feed concentration fitted well to a linear
 284 relationship ($R^2 > 0.99$) as demonstrated in Fig. 7a. We define the slope of this linear relationship as a
 285 salt production coefficient (k_t), which provides a fundamental parameter of this novel membrane pore
 286 storage process. Owing to the batch process characteristics, the salt production coefficients were

287 plotted against time as shown in Fig. 7b, using data from Fig. A2 in the Appendix where all $R^2 > 0.99$.
 288 After 20 min, NaCl accumulation in the pores reached saturation level (k_{sat}), suggesting an approach
 289 to equilibrium when the driving force is no longer significant. These results clearly indicate that the
 290 mass storage mechanism in the membrane pores of the hydrophilic inorganic membrane follows Eq.
 291 1 for a given condition, where P is the membrane surface specific salt production ($\text{mol}_s \text{m}^{-2}$), t is
 292 the pervaporation time, k is the salt production coefficient ($\text{mol}_s \text{L}_w \text{mol}_s^{-1} \text{m}^{-2}$) and c_f is the feed salt
 293 concentration ($\text{mol}_s \text{L}_w^{-1}$).

$$294 \quad P_t = k_t c_f \quad (\text{Eq. 2})$$

295



296

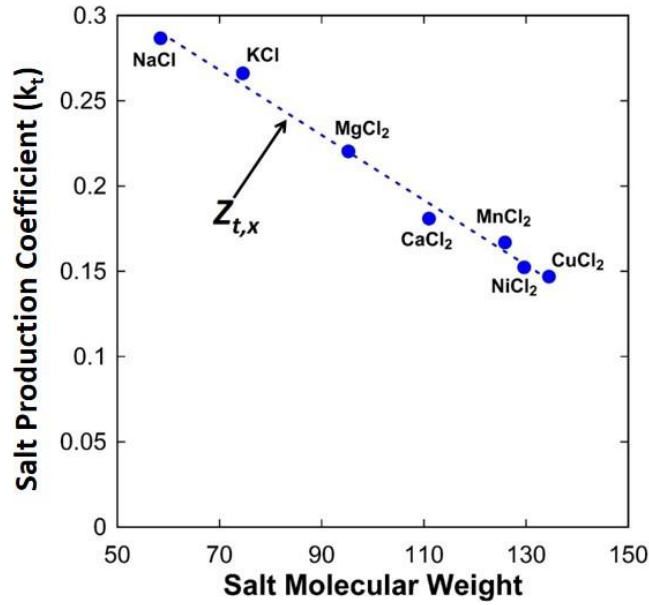
297 Fig. 7. (a) NaCl production versus feed concentration at 30 min pervaporation time, and (b) NaCl
 298 production coefficient (k_t) versus time.
 299

300 Another fundamental parameter for this novel pore storage mechanism is termed the global salt
 301 production coefficient (Z). The k_t values of the chloride salts in Fig. 8 derived from Fig. 4 were plotted
 302 against their molecular weights, excluding LiCl which slightly reacted with the membrane to some
 303 extent. Remarkably, the slope (Z) shows a linear relation (also $R^2 > 0.99$), clearly indicating that salt
 304 production is also a function of the molecular weight of the non-reactive chloride salts tested in this
 305 work. Therefore, Eq. 2 describes this property, where t is the pervaporation time, k is the salt

306 production coefficient and m is the molecular mass of salt x . The slope $Z=-317m_x+187$ for the
 307 chloride salts tested in this work.

308

309
$$k_{t,x} = Z_{t,x}m_x \text{ (Eq.3)}$$



310

311 Fig. 8. Global salt production coefficient ($Z_{t,x}$) for a series of non-reactive chloride base salts (3 mol
 312 L⁻¹ feed solutions at 20 °C) for a pervaporation time of 10 min and microwave drying at 900 W and
 313 2 min. Salt production coefficient includes hydrated salts.
 314

315 Essentially salt solutions were stored in the membrane during pervaporation, so the pore storage
 316 coefficients are volumetric as a function of the membrane surface area and membrane thickness.
 317 Hence, the mass storage coefficient (S_t) is the mass of salt mainly stored in the macropores of the
 318 substrate (mol_s m⁻² m⁻¹), per area (m²) per membrane thickness l (m), which can be derived from Eq.
 319 2 as follows:

320
$$S_t = \frac{P_t}{l} \text{ (Eq.4)}$$

321

322 Likewise, the global salt storage coefficient $GS_{t,x}$ for a membrane thickness l (m) can be derived from
 323 Eq. 3. As the slopes of $Z_{t,x}$ and $GS_{t,x}$ remain the same irrespective of the thickness of the membrane,

324 than both global salt production and global salt storage coefficients for chloride hydrates are the same
325 as follows:

$$326 \quad GS_{t,x} = Z_{t,x} \text{ (Eq. 5)}$$

327

328 In principle, the capability of the membrane to store salt is a function of the membrane specific
329 structure. Hence, salt production values increase by increasing the thickness of the substrate, or by
330 increasing the porosity of the substrate provided that membrane flooding is avoided. However, if
331 increased in salt production are proportional to the feed concentration and/or to the chloride salt
332 tested, then the slopes may remain the same. This means that the coefficients k_t and Z_t may not be
333 affected by the membrane's specific structure if salt production proportionality is maintained.

334

335 **4. Conclusions**

336 The induced crystallisation of mineral brines using hydrophilic inorganic membranes occurred via a
337 novel mechanism of membrane pore salt storage during pervaporation. This phenomenon occurred
338 due to the modulation of salt ion solution via the mesopores of titania and gamma-alumina layers,
339 thus avoiding pore flooding in the substrate macropores. Fundamental properties of the membrane
340 pore mass storage were established by determining salt production coefficient for single salts, and a
341 global salt storage coefficient as a function of the molecular weight of chloride salts. These
342 coefficients form the basis for the design of industrial plants for processing brines.

343

344 **Acknowledgement**

345 The authors acknowledge the financial support from the Australian Research Council
346 (DP1901002502) and (DP190101734) grants. J. C. Diniz da Costa gratefully thanks the support given
347 by the French "Centre National de la Recherche Scientifique" (CNRS-INC section 15) grant as
348 invited Professor at the Institut Européen des Membranes de Montpellier in France, and the Visiting

349 Fellowship d by the Associate Laboratory for Green Chemistry – LAQV, financed by the Portuguese
350 National Government funds from FCT/MCTES (UIDB/50006/2020).

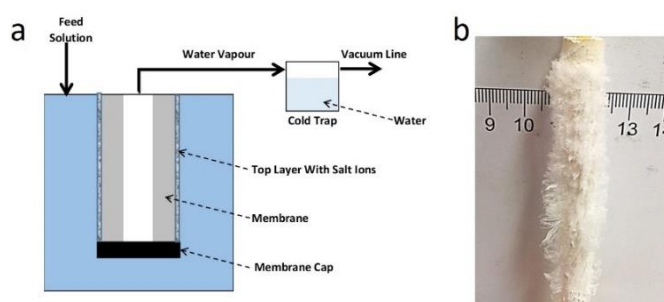
351

352 Competing interests

353 The authors declare no competing interests.

354

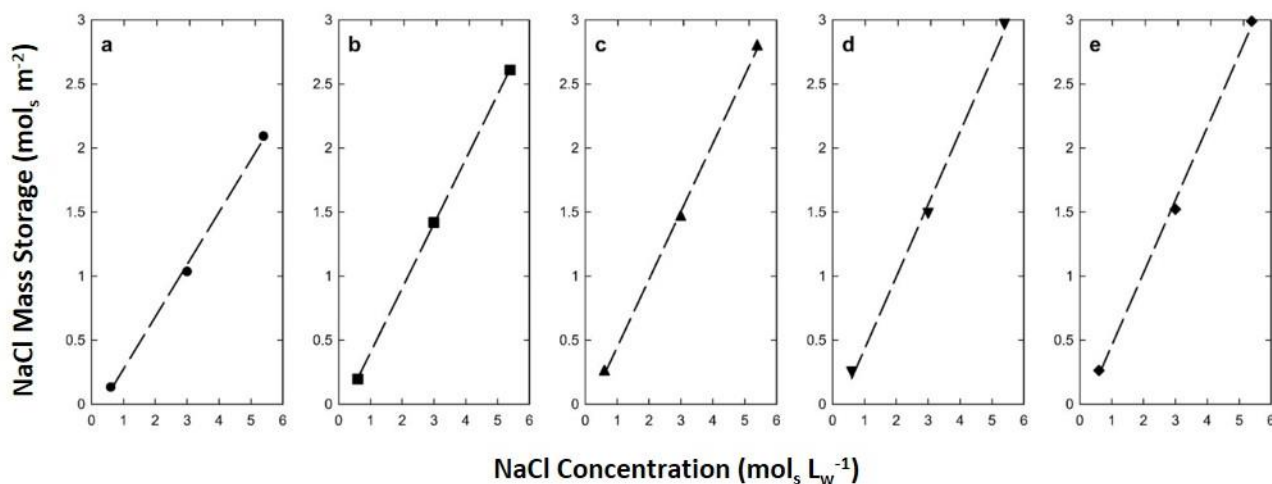
355 Appendix



356

357 Fig. A1. (a) Schematic of the pervaporation process and (b) image of an oven-dried membrane.

358



359

360 Fig. A2. Mass storage (average values) versus NaCl concentration for a series of pervaporation
361 times: (a) 10 min, (b) 15 min, (c) 20 min, (d) 25 min and (e) 30 min where all $R^2 > 0.99$.

362

363 The alpha-alumina substrate porosity of 36% was determined from helium pycnometry. The
364 substrate's pore volume (p_{vol}) is 675 mL for a membrane tube with a surface area of 1 m^2 , 1 cm outer
365 shell diameter and a wall thickness of 2.5 mm. Table 1 lists the average density (ρ) for the NaCl feed
366 concentrations used in this work. The NaCl densities were determined based soaking conditions of a

367 a membrane with 1 m² surface area with a solution in equilibrium with the feed temperature. The
 368 mass of salt (*M*) stored in the pores of the membrane is determined by $M = \rho p_{vol}$. Table A1 shows the
 369 NaCl mass stored mainly in the macropores of the substrates which are 99.96% of the total porosity.
 370 The NaCl production results from Fig. 3 are also listed. These results show that theoretical mass of
 371 NaCl stored in the substrate is always higher than the mass produced per 1 m² of membrane surface
 372 area.

373
 374 Table A1. Theoretical NaCl mass stored in the membrane pores for a membrane with 1 m² of surface
 375 area and pore volume of 675 mL.

Sol conc.	Sol conc.	Av. density	Membrane Mass sol	Membrane NaCl mass	Fig. 3 results NaCl mass
(mol _s L _w ⁻¹)	Wt%	(g L ⁻¹)	(g _{sol})	(g _s)	(g _s)
0.6	3.4	1022.3	690.4	23.5	16.2
3	14.9	1107.8	748.2	111.5	88.9
5.4	24	1180.4	797.2	191.3	174.0

376

377 References

- 378 1. Z. Fang, J. Wang, H. Wu, Q. Li, S. Fan, J. Wang, Progress and challenges of flexible lithium ion
 379 batteries, *J. Power Sources* 454 (2020) 227932.
- 380 2. T. Nemeth, P. Schröer, M. Kuipers, D.U. Sauer, Lithium titanate oxide battery cells for high-
 381 power automotive applications – Electro-thermal properties, aging behavior and cost
 382 considerations, *J. Energy Storage* 31 (2020) 101656.
- 383 3. M. Arbabzadeh, R. Sioshansi, J.X. Johnson, G.A. Keoleian, The role of energy storage in deep
 384 decarbonization of electricity production, *Nat Commun* 10 (2019) 3413
- 385 4. S.E. Kesler, P.W. Gruber, P.A. Medina, G.A. Keoleian, M.P. Everson, T.J. Wallington, Global
 386 lithium resources: Relative importance of pegmatite, brine and other deposits, *Ore Geology Rev.*
 387 48 (2012) 55-69.
- 388 5. U. Bardi, Extracting Minerals from Seawater: An Energy Analysis, *Sustainability* 2 (2010) 980-
 389 992.
- 390 6. U. Grober, J. Schmidt, K. Kisters, Magnesium in prevention and therapy, *Nutrients* 7 (2015)
 391 8199–8226.
- 392 7. S. Mahamuni, A.D. Lad, S. Patole, Photoluminescence properties of manganese-doped zinc
 393 selenide quantum dots, *J. Physical Chem. C* 112 (2008) 2271-2277.
- 394 8. C. Favero, M.B. Closs, G.B. Galland, R. Stieler, E. Rossetto, K. Bernardo-Gusmão, A binary
 395 nickel diimine-MCM-41 supported catalyst and its application in ethylene polymerization, *J.*
 396 *Catal.* 377 (2019) 63-71.
- 397 9. C. Zörb, M. Senbayram, E. Peiter, Potassium in agriculture – Status and perspectives, *Journal of*
 398 *Plant Physiology*, 171 (2014) 656-669..
- 399 10. S. Pacala, R. Socolow, Stabilization wedges: solving the climate problem for the next 50 years
 400 with current technologies, *Science* 305 (2004) 968-972.
- 401 11. D.S. Sholl, R.P. Lively, Seven chemical separations to change the world, *Nature* 532 (2016) 435-
 402 437.

- 403 12. E. Drioli, G. di Profio, E. Corsio, Progress in membrane crystallisation, *Curr. Opin. Chem. Eng.*
404 1 (2012)178-182.
- 405 13. C. A. Quist-Jensen, A. Ali, S. Mondal, F. Macedonio, E. Drioli, A study of membrane distillation
406 and crystallization for lithium recovery from high-concentrated aqueous solutions, *J. Membr.*
407 *Sci.* 505 (2016) 167-173.
- 408 14. X. Ji, E. Curcio, S. Al Obaidani, G. Di Profio, E. Fontananova, E. Drioli, Membrane distillation-
409 crystallization of seawater reverse osmosis brines, *Sep. Purif. Technol.* 71 (2010) 76-82.
- 410 15. G. Chen, Y. Lu, W. B. Krantz, R. Wanga, A. G. Fane, Optimization of operating conditions for
411 a continuous membrane distillation crystallization process with zero salty water discharge. *J.*
412 *Membr. Sci.* 450 (2014) 1-11.
- 413 16. W. Ye, J. Lin, Shen, P. Luis, B. Van der Bruggen, Membrane crystallization of sodium
414 carbonate for carbon dioxide recovery: effect of impurities on the crystal morphology, *Cryst.*
415 *Growth Des.* 13 (2013) 2362–2372.
- 416 17. L. Mariah, C.A. Buckley, C.J. Brouckaert, E. Curcio, E. Drioli, D. Jaganyi, D. Ramjugernath,
417 Membrane distillation of concentrated brines - role of water activities in the evaluation of
418 driving force, *J. Memb. Sci.* 280 (2006) 937-947.
- 419 18. E. Chabanon, D. Mangin, C. Charcosset, Membranes and crystallization processes: state of the
420 art and prospects, *J. Membr. Sci.* 509 (2016) 57–67.
- 421 19. J. Motuzas, C. Yacou, R.S.K. Madsen, W. Fu, D.K. Wang, A. Julbe, J. Vaughan, J. C. Diniz da
422 Costa. Novel Inorganic Membrane for the Percrystallization of Mineral, Food and
423 Pharmaceutical Compounds, *J. Membr. Sci.* 550 (2018) 407–415.
- 424 20. R.S. K. Madsen, J. Motuzas, A. Julbe, J. C. Diniz da Costa, Fine control of NaCl crystal size and
425 particle size in percrystallisation by tuning the morphology of carbonised sucrose membranes, *J.*
426 *Membr. Sci.* 567 (2018) 157-165.
- 427 21. R.S.K. Madsen, J. Motuzas, A. Julbe, J. Vaughan, J.C. Diniz da Costa, Novel membrane
428 percrystallisation process for nickel sulphate production, *Hydrometallurgy* 185 (2019) 210-217.
- 429 22. C. Yacou, S. Smart, J. C. Diniz da Costa, Mesoporous TiO₂ based membranes for water
430 desalination and brine processing, *Sep. Purif. Technol.* 147 (2015) 166-171.
- 431 23. A.F.M. Lenaars, A.J. Burggraaf, The preparation and characterisation of alumina membranes
432 with ultrafine pores. Part 2 - The formation of supported membranes, *J. Colloid Interface Sci.*
433 105 (1985) 27-40.
- 434 24. C.X.C. Lin, L. Ding, Simon K. Smart, J. C. Diniz da Costa, Cobalt oxide silica membranes for
435 desalination, *J. Coll. Interface Sci.* 368 (2012) 70–76.
- 436 25. A.F.M. Lenaars, K. Keizer, A.J. Bruggraaf, The preparation and characterisation of alumina
437 membranes with ultrafine pores. Part 1 - Microstructural investigation on non-supported
438 membranes. *J. Mater. Sci.* **19**, 1077-1088 (1984).
- 439 26. K.G. Kornev, A.V. Neimark, Spontaneous penetration of liquids into capillaries and porous
440 membranes revisited, *J. Coll. Interface Sci.* 235 (2001) 101–113.
- 441 27. K.W. Lawson, D.R. Lloyd, Membrane distillation, *J. Membr. Sci.* 124 (1997) 1-25.
- 442 28. V. Voronina, L. Pel, A. Sawdy, K. Kopinga, The influence of osmotic pressure on poulticing
443 treatments for cultural heritage objects, *Mater, Struct.* 46 (2013) 221-231.